Article

Not peer-reviewed version

3D Prospectivity Modeling of the Nibao Carlin-Type Gold Deposit, China: Insights into Mineralization Localization and Gold Exploration

Hui Guo , Xiancheng Mao * , Juexuan Huang *

Posted Date: 17 April 2024

doi: 10.20944/preprints202404.1143.v1

Keywords: Spatial Analysis; Mineral Prospectivity Modeling; Carlin-type Gold Deposit; Nibao Gold Deposit

Article

3D Prospectivity Modeling of the Nibao Carlin-Type Gold Deposit, China: Insights into Mineralization Localization and Gold Exploration

Hui Guo [1,2], Xiancheng Mao [1,*] and Juexuan Huang *

[1] Key Laboratory of Metallogenic Prediction of Nonferrous Metals and Geological Environment Monitoring Ministry of Education, School of Geosciences and Info-Physics, Central South University, Changsha 410083, China; amd21@163.com

[2] College of Forestry, Central South University of Forestry and Technology, Changsha 410004, China

* Correspondence: mxc@csu.edu.cn (X.M.); 225001042@csu.edu.cn (J.H.)

Abstract: Existing research indicates that mineralization of Carlin-type gold deposit is related to geological structures, but current studies mostly focus on the qualitative association, and lack quantitative analysis of the relationship between mineralization and structural features, which limits the potential for predictive mineral exploration. In this study, the Nibao Carlin-type gold deposit was selected as the research area to conduct three-dimensional geological modeling, spatial analysis, and three-dimensional prospectivity modeling. Spatial analysis revealed that the majority of gold ore bodies are situated near the main fault, with gold mineralization primarily occurring within a spatial range of approximately -80 meters to 20 meters from the main fault plane. This spatial distribution predominantly aligns in a SW-NE direction. Spatial characteristic extraction of fault slope indicators suggests that the slope angles are conducive to the migration and accumulation of ore-forming hydrothermal fluids, with ore body metal content rapidly increasing within an angle range of approximately 20° to 60°. The shape analysis of the mainfault indicates that the principal spaces of mineralization enrichment are within -10m to 20m of the fault plane undulations, where gold resources are concentrated in a relatively flat area. However, the degree of mineralization is more pronounced in the protruding sections than in the depressed areas. The areas with significant dip changes in faults display higher variations in orebody attitudes, with mineralization noticeably weaker in areas where the fault steepness changes markedly. Ore-bearing units exhibit significantly higher grades within the -17° to 3° interval of fault steepness transition. This interval also sees a rapid accumulation of gold resources. The Nibao gold mine's mineralization is derived from deep, ore-bearing hydrothermal fluids ascending along major fractures, precipitating, and accumulating in favorable ore-hosting spaces (faults, anticline cores) and lithological combinations (sedimentary tuffs, tuffs). Three deep potential gold targets were identified, highlighting the deep western edge of the F1 fault and the deep southeast-trending lower plate as prospective areas for future exploration. This study underscores the effectiveness of 3D prospective modeling as an indispensable tool for elucidating the spatial distribution of fault-controlled Carlin-type gold deposits and their tectonic determinants.

Keywords: spatial analysis; mineral prospectivity modeling; Carlin-type gold deposit; Nibao gold deposit

1. Introduction

It is widely recognized that the genesis of Carlin type gold deposits is closely related to structural activities. These deposits commonly form at the intersections between faults and permeable reactive strata, situated beneath impermeable cover layers. They are often marked by carbonate dissolution and micron-sized diagenetic alteration of leached pyrite. Carlin-type deposits are typically extensive and of low grade, exhibiting a clustered and zoned distribution. The host rocks for the mineralization predominantly consist of carbonaceous siltstones or carbonates undergoing processes such as decarbonization and silicification (frequently associated with mineralization), or argillization [1,2].

 doi:10.20944/preprints202404.1143.v1

are important, thus, it is critical for identifying the spatial correlation betweenCarlin-type gold mineralization and structures as well as understanding how structural activities drive the migration and accumulation of auriferous fluids [4].

The conceptual model for the origin of Carlin-type deposits has transitioned from being perceived as shallow hydrothermal deposits linked with Tertiary magmatism [5], through to interpretations as deep metamorphic deposits [6], and finally to being viewed as hydrothermal deposits situated at intermediate depths [7]. These deposits are posited to have originated at shallow depths (< 3 km) between 42-34 Ma, formed by low-salinity, low-temperature fluids in magmas from deep significant fractures, concurrent with the shift from extrusion to extension dynamics. The depth range of Carlin-type deposits, as inferred from major faults, is generally in the order of several kilometers. Hofstra and Cline noted that Carlin-type deposits typically formed at depths of less than 2 km [7], although earlier investigations [8] posited deeper formation levels. Some pre-mineralization stages in Carlin-type gold deposits are hypothesized to have occurred at depths up to 4 km [9,10]. Moreover, considerable debate persists regarding the key indicators of Carlin-type gold genesis and the origins of the mineralizing fluids [11,12]. The mineralization contexts and factors of the Carlin-type gold mines in Qianxinan exhibit significant deviations from the “standard” Carlin-type gold mines in the U.S. According to traditional gold mine classification standards, the Carlin-type gold mines in Qianxinan might be categorized as an “intermediate” type, serving as a transitional variant between Carlin-type and orogenic gold mines, especially in terms of mineralization temperature, pressure, and chemical properties. However, there is relatively little quantitative understanding of the spatial correlation between the structures and mineralization in the Nibao deposit, which limits the precise mineral prospectivity of concealed orebody.

Presently, the method of 3D mineral prospectivity modeling is widely applied in the quantitative analysis of ore-controling factors and mineralization, and has achieved remarkable results in accurately positioning ore bodies and revealing the genesis of deposits. 3D spatial analysis has been demonstrated as an effective approach for identifying the spatial features of geological objects in 3D space and extracting diverse potential ore-controlling features for 3D prospectivity modeling [15–18]. Prospectivity modelingcan integrate the non-linearity and high-dimensionality spatial association between ore and ore-controlling features [18]. Therefore, 3D mineral prospectivity modeling is a potential tool for determining the quantitative relationship between mineralization and structure in Carlin type deposits.

The Nibao gold deposit exemplifies a structurally controlled hydrothermal deposit. Utilizing the deposit’s drilling data and geophysical profiling, we constructed a three-dimensional geometric model encompassing the F1 fault, ore body, designating this model as a key piece of prospective evidence. Subsequent spatial analyses of the geological features were conducted to quantitatively extract evidence layers regarding structural characteristics. Leveraging these outcomes, Artificial Neural Network techniques were applied to amalgamate spatial data into predictive models, aiming to minimize errors and biases. The specific objectives of this study are: (1) to delineate the geometric characteristics of faults within the Nibao gold deposit; (2) to quantify the linkage between fault geometry and gold mineralization; (3) to pinpoint areas of potential gold mineralization; (4) to furnish novel insights into the structural control mechanisms governing fault-controlled Carlin-type gold deposits in southwestern Guizhou.

2. Geological Background

The Nibao Carlin-type gold deposit is located at the intersection of the Yangtze quasi-platform and the western of the Youjiang fold [19].

 doi:10.20944/preprints202404.1143.v1

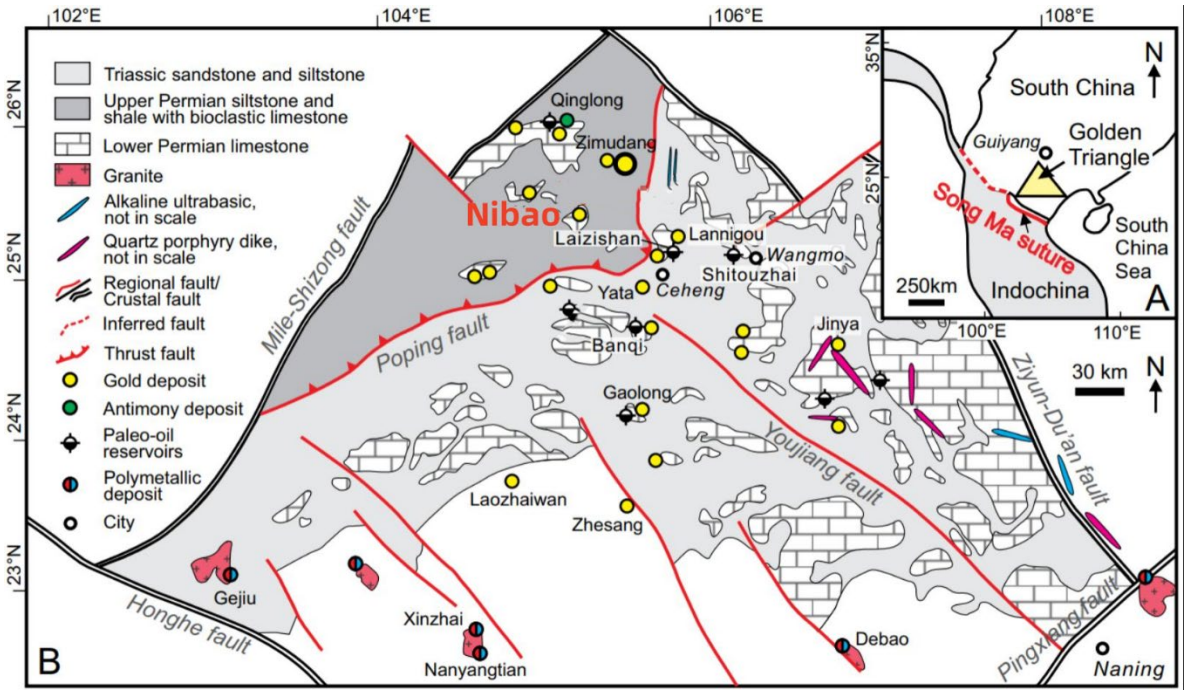

Figure 1. Tectonic Location of the Youjiang Basin (A) Geological Map of the Youjiang Basin (B) (modified from Li., 2021).

The region is situated within the "triangular" [20] block demarcated by the northeast-trending Maitreya-Shizong Deep Fault, the northwest-trending Ziyun-Yadu Deep Fault, and the nearly east-west trending Kaiyuan-Pingtang Deep Fault. This area lies at the northwest apex of the "Golden Triangle" in Yunnan, Guizhou, and Guangxi. A cluster of mineral deposits, including Yata, Getang, Shaguochang, and Nibao, forms the "Carlin-type" gold deposit concentration zone in southwestern Guizhou. The bedrock geology predominantly consists of Archean and Proterozoic metamorphic rocks, such as gneiss, quartz diorite, and gneissic monzonite. Overlying these basement rocks are Paleozoic strata, chiefly comprising Ordovician and Silurian carbonate rocks, shale, and sandstone. These layers underwent folding and fracturing due to later tectonic activities, leading to the deformation and fracturing of the strata. The locality encompassing the Nibao gold deposit also experienced the impacts of Yanshanian tectonic movements, which resulted in crustal deformations including uplift, compression, and fracturing, thereby shaping the mountains and tectonic faults in the region [21,22].

The structural framework of the Nibao gold deposit is predominantly characterized by faults and folds, with the F1 reverse fault playing a crucial role as the primary ore-controlling structure [23–25]. Spanning nearly the entirety of the mining area, F1 extends approximately 5.50 km. Its eastern terminus is located at the red rock, where it intersects with the F3 fault, while its western limit is truncated by the F6 fault near Shimenkan's west before concluding at the F1 fault. South of Zhujue, it meets the F12 fault. The fault's orientation shifts from north-northeast (70-85°) to the west of Yujiaping, gradually transitioning to northeast (40-20°) towards the east, and inclines south-southeast, with a dip angle ranging from 20-42° (with the mining section ranging from 20-35°). This fault structure serves as the principal focus of this study.

Preprints.org (www.preprints.org) | NOT PEER-REVIEWED | Posted: 17 April 2024 doi:10.20944/preprints202404.1143.v1

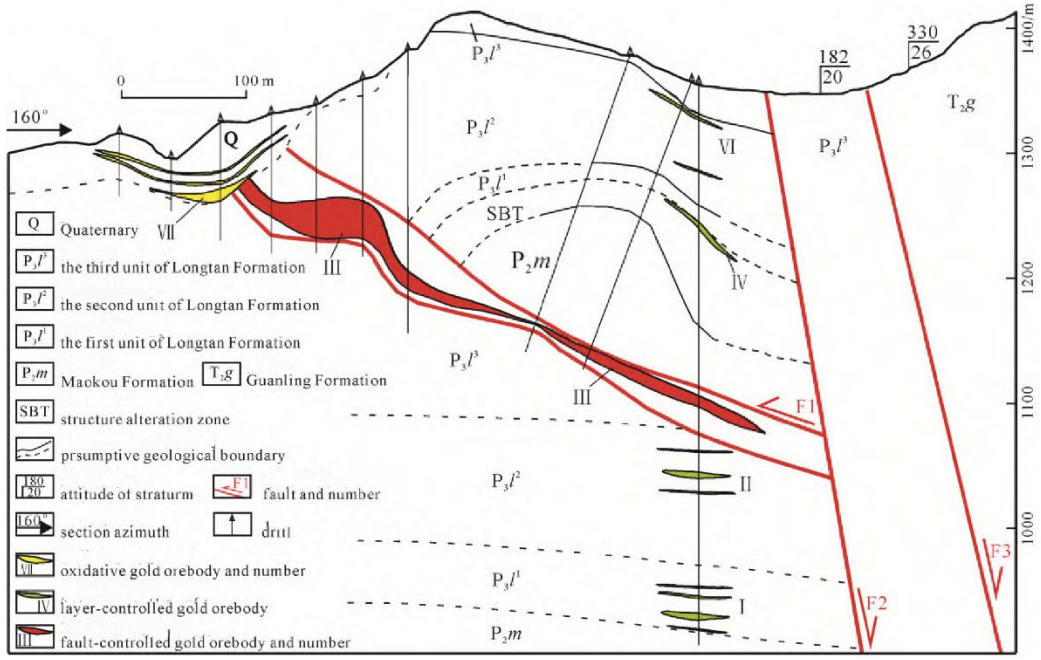

Figure 2. Profile of exploration line 9460 in Nibao gold deposit, Guizhou Province (modified from Liu 2014, and Zheng, 2017).

The Nibao gold deposit comprises both oxidized and primary ores. The substantial ore bodies, such as No. III and No. IV, are under the direct influence of the F1 fault. The No. III ore body's host rocks include gravel sandstone, silty claystone, sedimentary tuff, and limestone, all of which exhibit pronounced silicification and pyrite alteration, characteristic of a primary mine. The orientation of the ore body aligns closely with the fault's orientation, displaying a general dip angle of 20-35° with gentle undulations, and manifesting in either a plate-like or lens-like morphology. The ore body demonstrates phenomena of expansion, contraction, branching, and compounding, and is located at an elevation ranging from 955.66 to 1307.41 meters. The average core drilling thickness is 6.02 meters, with an average gold grade of 3.42 g/ton. Similarly, the No. IV ore body's host rocks are primarily thin to medium-bedded sedimentary tuffs, also exhibiting significant silicification and pyrite alteration indicative of a primary mine. The morphology and orientation of the ore body correspond with the shape and orientation of the Sbt alteration body, situated at elevations between 1120.74 and 1509.66 meters. This ore body has an average core drilling thickness of 5.67 meters and an average gold grade of 3.63 g/ton. The ore presents in dark gray, gray, and black hues, characterized by a relatively complex material composition with a prevalence of metal sulfides, including pyrite and arsenopyrite. The ore's texture is comparatively hard, with gold predominantly occurring as electrum.

3. Method

3.1. 3D Geological Modeling

The comprehensive geological data collected in this study include a 1:250,000 Nibao exploration area regional geological map, a 1: 10,000 scale surface geological map, 15 1:1000 cross sections, 294 1: 200 drill holes and other data. These datasets were provided by Guizhou Provincial Bureau of Geology and Mineral Exploration and Development (Guiyang, China).

We initiated our methodology by developing precise and comprehensive wireframe models through meticulous manual digital construction utilizing ArcGIS and SKUA-GoCAD. This process was grounded on borehole data and cross-sections within regions characterized by high data density. Subsequently, an implicit modeling approach was employed to fabricate a 3D surface model of the

 doi:10.20944/preprints202404.1143.v1

Nibao fault (Figure 6). The outcomes of the modeling encompass nearly all discernible general structural trends observable on the Nibao fault [26].

To enhance the representation of mineralization spatially, both surface and wireframe models of the ore body were voxelized into block models, with each voxel assigned graphical attribute information (e.g., grade, position, among others). A 3D Kriging interpolation method [15,27–34] was utilized to determine the gold grade for each voxel, leveraging 20,045 available gold assay results.

Table 1. variogram parameters resulting from Nibao Gold deposit.

Nugget	Sill	Variation range (m)	Azimuth (°)	Dip Direction (°)	Dip Angle (°)
0.834	0.068	250.00	140.00	45.00	89.9015

3.2. Spatial Analysis

The objective of this analysis is to quantify and assess the impact of various factors on the mineralization process [35–38], as well as to elucidate the relationship between structural features and mineralization. By conducting distance field analysis, slope analysis, Morphological analysis, and analysis of The dip variation within the Nibao gold deposit, we aim to achieve a comprehensive understanding of the determinants influencing gold mineralization.

Distance analysis utilizes the spatial relationship between the fault and adjacent geological entities to delineate the features and structural attributes of the fracture surface by computing the distance field. This method involves examining the relationship between fault and geological objects through the observation of changes, gradients, and spatial distribution patterns within the distance field [39–42]. Such analysis can elucidate the connectivity of fault, the interconnections among fracture segments, and the dynamics of fracture networks. The convention sets the hanging wall unit as exhibiting a positive distance, while the footwall unit is assigned a negative distance. This assigns the position of the unit's center point (x_v, y_v, z_v).Consequently,when a point(x_v, y_v, z_v).. resides on the fracture surface, the assigned value is positive; conversely, when a point $(x_v, y_v, z_v)$is situated in the footwall of the fracture surface, the value is deemed negative. $dF = \pm\min\left[\sqrt{(x-x_v)^2+(y-y_v)^2+(z-z_v)^2}\right]$ .In the equation ,(x_v, y_v, z_v) represent the spatial coordinates of the center point of the gold ore body unit. To analyze profile data on a designated fracture surface, one or more profile lines are selected across the fracture surface, and elevation changes along these lines are measured. Subsequently, the profile slope of the fracture surface is determined based on the gradient of elevation change along the profile line. This profile slope offers insights into the fracture surface's inclination and variations. Distinct from the fault's dip angle, the slope provides a more localized reflection of changes in the fracture surface's orientation. By calculating elevation values at various points on the fault surface and analyzing elevation change patterns, the structural slope of the fault surface can be deduced. The equation of any $\triangle$ABC of the TIN model can be expressed as $z = ax + by + c$.To calculate the slope α, just substitute a and b in the formula into the formula $\alpha = \arccos\frac{1}{\sqrt{a^2+b^2+1}}$.

The transition between steep and gentle inclinations within the Nibao gold deposit's metalorganic structure marks a critical juncture where the behavior of ore-forming hydrothermal fluids is notably altered. At this juncture, the fluids may either experience abnormal migration or encounter a barrier that halts their further movement, prompting them to accumulate at this site. This phenomenon contributes to the formation of a distinct steep-to-gentle transition in the metallogenic structure, effectively illustrating the ore control effect of this structural feature. The spatial manifestation of the mineralization structure's surface can be leveraged to elucidate this influence on ore deposition.

Preprints.org (www.preprints.org) | NOT PEER-REVIEWED | Posted: 17 April 2024 doi:10.20944/preprints202404.1143.v1

$Z = f(x,y) = ax^3 + bx^2y + cxy^2 + dy^3 + ex^2 + fxy + gy^2 + hx + iy + j$ to represent. write it down as $Z = f(x,y) = \boldsymbol{a}^{\mathrm{T}}\boldsymbol{x}\,\boldsymbol{a}^{\mathrm{T}} = [a \quad b \quad \cdots \quad j]$, $\boldsymbol{x} = [x^3 \quad x^2y \quad \cdots \quad 1]^{\mathrm{T}}$, $\boldsymbol{x} = [x^3 \quad x^2y \quad \cdots \quad 1]^{\mathrm{T}}$.The local surface analytical formula can be obtained according to the least squares method. The fitting method is as follows $Z = f(x,y) = \min_{|\boldsymbol{a}|} \sum_{i \in N(x,y)} W(x_i,y_i) \| \boldsymbol{a}^{\mathrm{T}}\boldsymbol{x}_i,\ Z_i \|$ .in the formula , $N(x,y)$ is the neighborhood range of point (x,y) , $W(x_i,y_i)$ efers to the weight of point$(x_i,y_i)$to the current point (x,y) O be found, which can be determined by the geographical weighted regression method , $\|a,\ b\|$ is the L2 norm of a , b, that is, a, b Euclidean distance between. Obtaining a determines the local analytical formula of the structural surface $\boldsymbol{a}_{(x,y)} = (\boldsymbol{X}^{\mathrm{T}}\boldsymbol{W}\boldsymbol{X}^{\mathrm{T}})^{-1}\boldsymbol{X}^{\mathrm{T}}\boldsymbol{W}\boldsymbol{z}$.

in the formula , $\boldsymbol{X}^{\mathrm{T}} = [\boldsymbol{x}_1^{\mathrm{T}} \quad \boldsymbol{x}_2^{\mathrm{T}} \quad \cdots \quad \boldsymbol{x}_n^{\mathrm{T}}]$, $\boldsymbol{z}^{\mathrm{T}} = [\boldsymbol{z}_1 \quad \boldsymbol{z}_2 \quad \cdots \quad \boldsymbol{z}_n]$, $\boldsymbol{W} = \begin{bmatrix} W_{x,y}(x_1,y_1) & & & \\ & W_{x,y}(x_2,y_2) & & \\ & & \ddots & \\ & & & W_{x,y}(x_n,y_n) \end{bmatrix}$.

Upon establishing the local surface analytical expression of the mineralization structure, it becomes possible to compute the intensity value of the steep-to-gentle transition. This transition specifically pertains to the intensity of variation within the structural orientation, necessitating the calculation of the second-order directional derivative of the surface's analytical expression at the specified point (with the first order representing the slope). The process is as follows:

$$\left.\frac{\partial^2 f(x,y)}{\partial n^2}\right|_{\substack{x=0\\y=0}} = \frac{a^2 \left.\frac{\partial^2 f(x,y)}{\partial x^2}\right|_{x=0} + 2ab \left.\frac{\partial^2 f(x,y)}{\partial x \partial y}\right|_{\substack{x=0\\y=0}} + b^2 \left.\frac{\partial^2 f(x,y)}{\partial y^2}\right|_{y=0}}{\partial n^2}$$

In the formula, the coordinate system is the local coordinate of the point to be found, that is, x=0, y=0 is the point to be found. As just mentioned, the first directional derivative of the structural surface is the slope, that is $\frac{\partial^2 f(x,y)}{\partial n^2} = \frac{\partial\left(\frac{\partial f(x,y)}{\partial n}\right)}{\partial n} = \frac{\partial \tan\theta}{\partial n} = \frac{\partial \tan\theta}{\partial \theta}\frac{\partial \theta}{\partial n}$. In the formula, θ is the inclination angle (slope angle) of the structural surface at the point to be found. It should be noted that $\partial\theta/\partial$n represents the intensity of the change in structural orientation, namely, the steep-to-gentle transition intensity value.

$$\left.\frac{\partial \theta}{\partial n}\right|_{\substack{x=0\\y=0}} = \frac{\partial^2 f(x,y)}{\partial n^2}\frac{\partial \theta}{\partial \tan\theta} = \left.\frac{\partial^2 f(x,y)}{\partial n^2}\right|_{\substack{x=0\\y=0}} \frac{1}{(\tan\theta)'},$$

By substituting the result of $\frac{\partial^2 f(x,y)}{\partial n^2}$ By inserting the results and the dip angle (slope angle) into the preceding formula, the steep-to-gentle transition intensity value$\frac{\partial \theta}{\partial n}$ can be calculated.

The shape of the fault surface plays a significant role in controlling the ore within the geological space surrounding the fault surface. By examining the concave and convex features of the fracture surface, insights into the structural background and controlling factors influencing mineral deposit formation can be gained. This process allows for the quantitative expression of the convexity and concavity degree on certain sections of the geological body surface. By adjusting the radius of the interpolation search range, different levels of trend undulations can be discerned. The undulation of the fault surface significantly influences ore control within the geological space surrounding the fault. Analyzing the concave and convex features of the fracture surface uncovers the structural background and factors controlling mineral deposit formation. This involves identifying and segregating trends and fluctuations within the data. Based on the fault's size and the exploratory project's network density, a 100-meter radius is designated for the interpolation search range, leading to the smoothing of the original data. Morphological filtering of the fracture surface is conducted to delineate the trend shape; subsequently, distances from units within both the convex and concave sections to the trend shape's outline are calculated. This enables the quantitative expression of the convexity and concavity degrees on specific sections of the geological body surface. By adjusting the

 doi:10.20944/preprints202404.1143.v1

radius of the interpolation search range, trends and fluctuations at various levels can be discerned. $waF(x_v, y_v) = O(x_v, y_v) - T(x_v, y_v)$ .Here, $O(x_v, y_v)$ epresents the elevation value of the point with coordinates (x_v, y_v)in the TIN model of the original primary fracture surface O, and $T(x_v, y_v)$is the elevation value of the corresponding point on the trend surface T. Thus, when the value of $wF(x_v, y_v)$is positive, it indicates an uplift at this point on the fracture surface; a negative value signifies a depression. The process of determining the trend surface involves using the ID numbers of the TIN model points as indexes, setting a filtering window of a specified size for each point, and calculating the average elevation value of all points within the range, specifically as $T(x_v, y_v) = \frac{\sum_{i=1}^{n} \frac{O(x_i, y_i)}{d_i^2}}{\sum_{i=1}^{n} \frac{1}{d_i^2}}$. In this formula, n is the number of points within the filtering search radius; $O(x_i, y_i)$is the elevation value of the point with coordinates(x_i, y_i) in the TIN model of the original primary fracture surface O, and $T(x_v, y_v)$is the elevation value of the corresponding point on trend surface,d_i is the Euclidean distance from point (x_v, y_v) to point(x_i, y_i) Based on the actual subject of study, the uplift and depression of the fracture surface at different scales were examined to determine the trend surface T_1, with the filtering radius set to 100 m during the generation of T_1. T_1 focuses more on the local morphological features of the fracture surface, hence the formula is further refined to $waF(x_v, y_v) = O(x_v, y_v) - T_1(x_v, y_v)$ is the elevation value of the point with coordinates (x_v, y_v)in the TIN model of the original primary fracture surface O, and $T_1(x_v, y_v)$s the elevation value of the corresponding point on trend surface.

 doi:10.20944/preprints202404.1143.v1

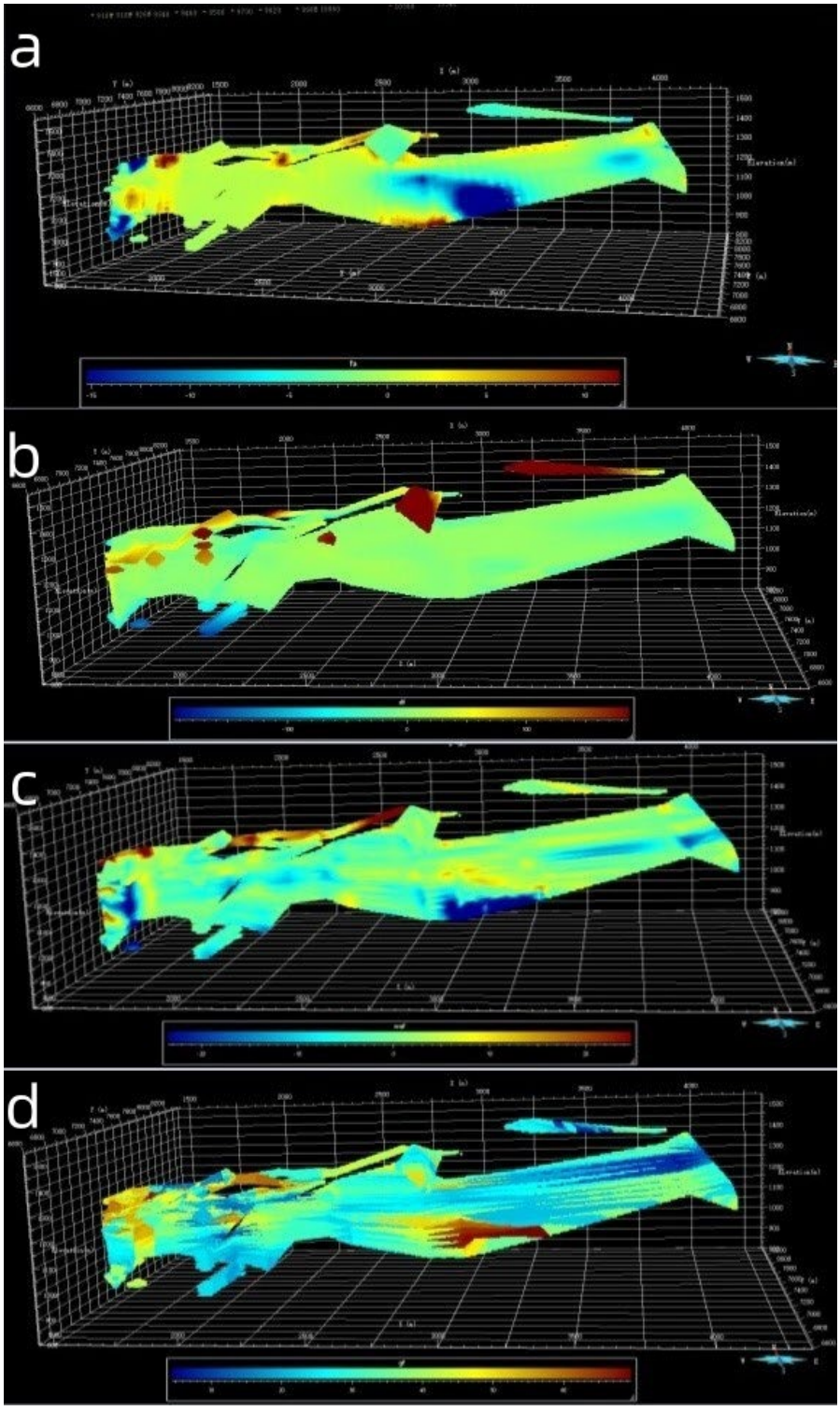

Figure 3. 3D models showing the effects of the Nibao fault's geometric attributes on known voxels: geometric attributes on known voxels: (a slope (dip angle gF); b distance (dF) where negative values on the scale are in the footwall; c undulations (waF); and d dip angle changes (fV).

3.3. Mineral Prospectivity Modeling

which regards the spatial information as multivariate features [15,36,39] Unstructured data was adeptly processed using Artificial Neural Network Model algorithms to unveil the obscured relationships between structure and mineralization. [43–46]

 doi:10.20944/preprints202404.1143.v1

The Multilayer Perceptron (MLP), a widely implemented artificial neural network model, is adept at addressing both classification and regression challenges. It comprises multiple layers of neurons, including an input layer, one or more hidden layers, and an output layer. The architecture of an MLP—such as the number of neurons in the input layer, the count and size of hidden layers, and the number of neurons in the output layer—is tailored based on the problem's complexity and the data's characteristics. Initial values for all connection weights and bias terms are set using methods like random or normal distribution initialization [47–49].

During forward propagation, the neural network's output is computed as input features traverse from the input layer through the hidden layers to the output layer. Each neuron processes inputs from the preceding layer, applying weights and biases, before passing the result to the next layer. Nonlinear transformations are introduced via activation functions (e.g., ReLU, Sigmoid, tanh). The weight matrices link the input layer to the hidden layer and the hidden layer to the output layer, with the output value derived after applying the activation function [50].

The MLP employs the error backpropagation algorithm, coupled with gradient descent for weight updates, to refine the weight matrices across layers. This iterative process aims to minimize the discrepancy between the network's output and the actual target output, enhancing the correlation between input features and desired outcomes. Through non-linear activation functions in the hidden layers, MLPs can model complex non-linear relationships, offering superior performance over simple linear models [51]. They are versatile, suitable for various machine learning tasks like classification, regression, and clustering, with adjustable structures to accommodate different data sets and objectives [52]. However, the complexity of MLPs necessitates substantial data and computational resources for training and fine-tuning, with attention required to avoid overfitting and to mitigate the impact of initial weight settings on training efficacy and convergence rates. $\boldsymbol{h_1} = S(\boldsymbol{W_1 x_i} + \boldsymbol{b_1})$, $\boldsymbol{h_2} = S(\boldsymbol{W_2 h_1} + \boldsymbol{b_2})$, $\boldsymbol{h_3} = S(\boldsymbol{W_3 h_2} + \boldsymbol{b_3})$ $\boldsymbol{o} = \boldsymbol{W_4 h_3} + \boldsymbol{b_4}$. Among them, $\boldsymbol{x_i}$is the input feature, $\boldsymbol{W_i}$、$\boldsymbol{b_i}$and$\boldsymbol{h_i}$are the weight matrix, bias and output of each hidden layer, $\boldsymbol{o}$is the network output, and $S$is the sigmoid activation function: $S(t) = \frac{1}{1+e^{-t}}$.

When using a multi-layer perceptron model to correlate mineralization indicators and prospecting information indicators, the objective function (mean square error) is: $E = \frac{1}{2}\sum_{x_i \in GV, y_i \in MV} \| f(x_i) - y_i \|_2$

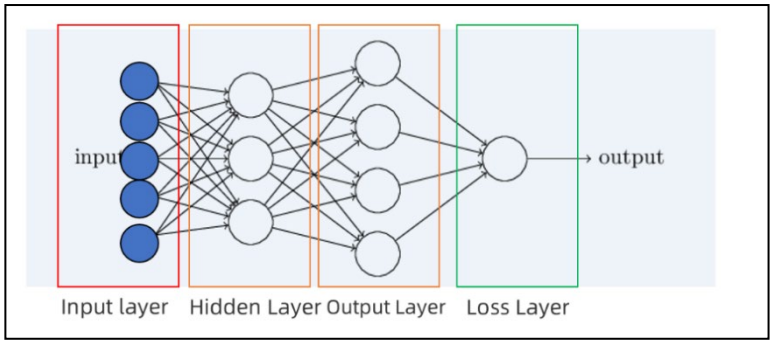

Figure 4. The diagram displays the architecture of a multilayer perceptron deep neural network, which includes an input layer and hidden layers.

In the context, y_i represents the actual output corresponding to inputx_i. During the training phase of the multilayer perceptron model, the error backpropagation algorithm utilizes the gradient descent strategy [53–55]. This involves adjusting the network's weights in the direction opposite to the gradient of the objective function. Training concludes once the objective function has been minimized to an optimal extent. The Receiver Operating Characteristic (ROC) curve serves as a graphical tool for analyzing binary classification models [56]. Within the ROC space, the False Positive Rate (FPR) is designated as the x-axis, and the True Positive Rate (TPR) occupies the y-axis. The significance of the Area Under the ROC Curve (AUC) encompasses the following points: AUC values range from 0 to 1, predicated on the assumption that values above a certain threshold are classified as positive, while those below are deemed negative. Furthermore, if a positive and a

 doi:10.20944/preprints202404.1143.v1

negative sample are randomly chosen, the AUC represents the probability that the classifier will correctly assign a higher score to the positive sample over the negative one [57]. Consequently, a larger AUC value indicates greater accuracy of the classifier.

4. Results

4.1. Spatial Distribution of Gold Mineralization

The 3D models show that gold orebodies of the Nibao deposit consist of large numbers of small ore lenses that are generally discontinuous in space (Figure 5). They dip to the SE and extend from near surface to more than 400m depth. Gold mineral-ization is confined to gently undulating, roughly parallel zones in the foot-wall of the F1 fault. The results of gold grade estimation for the Nibao orebodies reveal that ore voxels (>0.5 g/t)have grades of <4 g/t with mean of 0.83. Gold spatial distribution is markedly uneven, such that high-grade ore bodies (>4 g/t) are distributed mostly in the 1300m to 1000m levels, where the most dominant gold resources are concentrated (Figure 5). In map view, major gold mineralization is found in the western part of the modeled area (Figure 5).

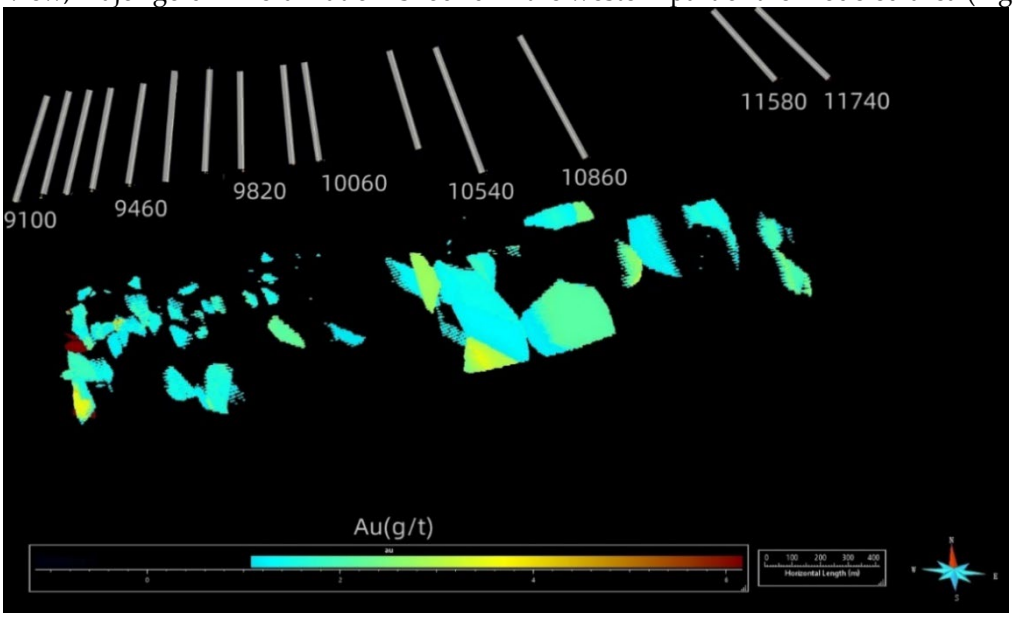

Figure 5. 3D assay models shown in grams per ton, Bar chart showing gold resources in the modeled volume from west to east across the map. Voxels with Au grade<0.5 g/t are not shown in models.

4.2. Structural Deformation in A 3D View

Based on the morphological features of the three-dimensional model and ancillary exploration data, the F1 thrust fault is observed to have developed from SW to NE during the mid to late Yanshanian period, associated with mineralization processes. The F1 fault emerges as the principal ore-controlling and ore-hosting structure of the Nibao Carlin-type gold deposit, playing a pivotal role in guiding the main ore-depositing activities [58]. The interlayer fracture zone that formed within the footwall during the F1 fault's development serves as a secondary ore-controlling factor. Collectively, the primary faults, fissures, and stratigraphic lithology intricately influence the formation and eventual morphology of the ore body in the Nibao Gold deposit [59]. This underscores the thrusting activity along the F1 fault as the dominant condition influencing mineralization.

4.3. Correlation between Gold and Structural Features

Spatial distance analysis reveals that gold primarily resides in the footwall of the Nibao F1 fault, within a range of -80m to 20m. Through distance field analysis, two gold-enriched zones were identified, with a concentration of high-grade ore bodies predominantly in the lower section of the fault's crush zone, and a secondary enrichment in its upper section. This distribution pattern flanks

 doi:10.20944/preprints202404.1143.v1

both sides of the fault crush zone, indicating a bimodal distribution across the main fault's mineralization enrichment areas (refer to Figure 6a). Analysis of the fault slope index's spatial characteristics demonstrates uneven spatial distribution of slope, suggesting notable variations in mineralization. A significant peak in the mineralization index is observed within the slope range of 20° to 60°, with higher or lower slope factors forming in an irregular strip-like pattern. The mean and median values stand at 33.1538 and 29.5400, respectively. As depicted, metal content and mineralization index share similar peak distribution ranges, with secondary peaks in areas of steeper slopes (see Figure 6b). This highlights the slope angle's role in facilitating the movement and accumulation of ore-forming hydrothermal fluids, with rapid metal content accumulation noted in the 20° to 60° range (Figure 6b), indicating a concentration of ore bodies within this characteristic slope range. Quantitative analysis results (Figure 6d) suggest that gold resources are densely concentrated in areas with minor fluctuations. As the trend fluctuation value increases, the mineralization index value sharply declines, with stronger mineralization observed in depressions than in protrusions. The accumulated metal amount surges within the -10m~20m range of the fracture surface, plateauing beyond the 20-meter mark. The steep and gentle transition indicator's higher or lower positioning signifies the transition intensity. The transition between steep and gentle areas on the main fault surface reveals numerous ore body units in sections with minimal transition. Notably, two locations exhibit significant steep and gentle transitions, where the ore bodies display higher yield changes (Figure 6b).

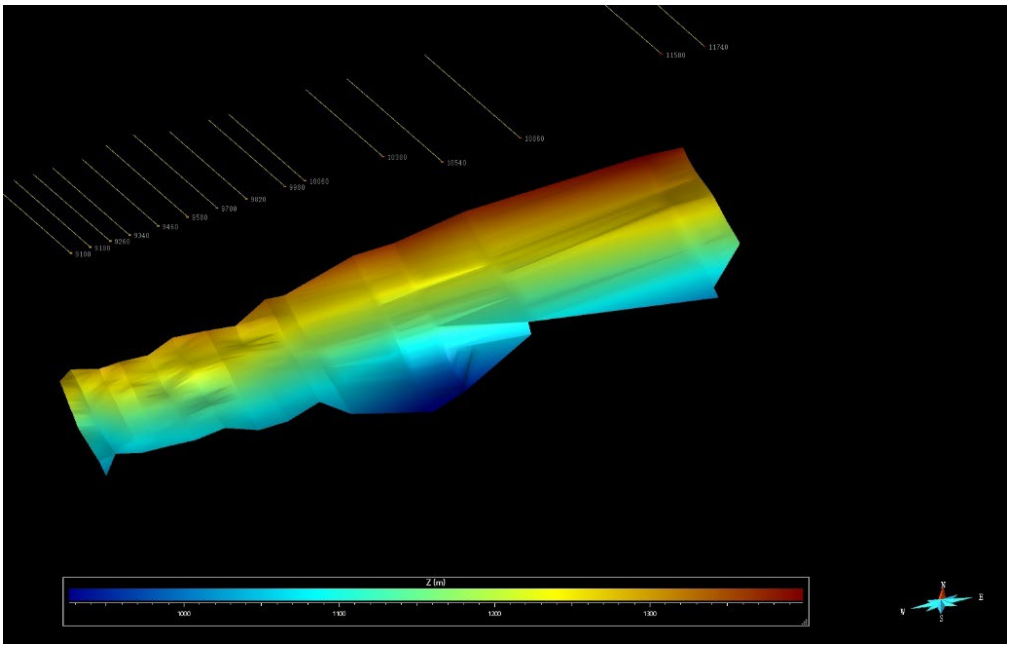

Figure 6. The F1 fault of the Nibao gold deposit.

Statistical analysis indicates a high degree of aggregation for *f*V, with mean and median values approximately at -5.5°. In the histogram correlating the fault steepness change factor (*f*V) with ore body grade (Au), ore-bearing units within the steepness transition value range of -17°~3° exhibit distinctly higher grades. This interval also sees rapid gold resource accumulation (Figure 6b), with a singular peak accumulation phenomenon near the zero transition value. A robust correlation exists between mineralization distribution and the steep-to-gentle transition *f*V, showcasing a unimodal distribution of metal content under steep and gentle transition *f*V. Metal content enriches near the zero value of the main fault's steep and gentle transition fV, indicating locations where fracture occurrences are relatively continuous and exhibit minimal change. The more consistent the fracture surface, the richer the mineralization, with the *f*V value in the -17°~3° range predominantly controlling metal output.

Preprints.org (www.preprints.org) | NOT PEER-REVIEWED | Posted: 17 April 2024 doi:10.20944/preprints202404.1143.v1

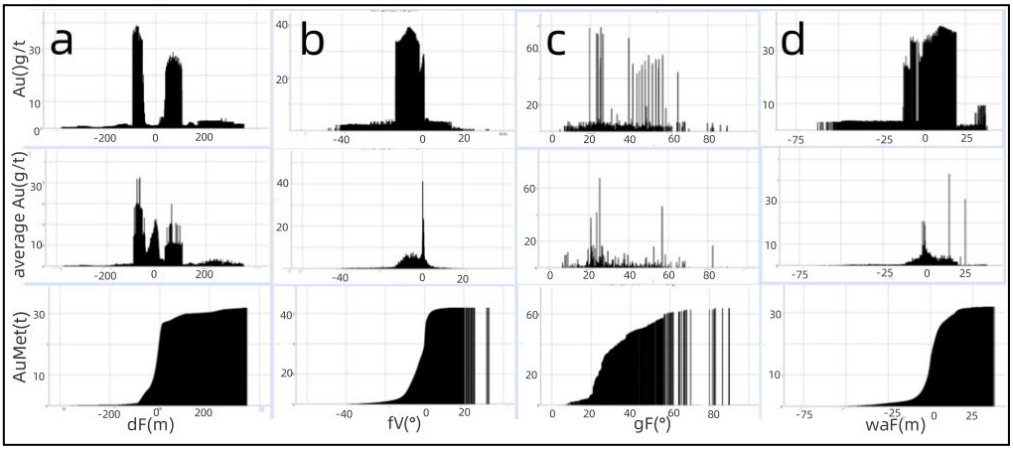

Figure 7. The association between the geometric features of the Nibao fault and the extent of gold mineralization is illustrated as follows: a) Sequentially, from top to bottom, the panels depict the correlation between the distance to the fault (*d*F) and the gold grade, the metal content, and the aggregate gold resources (AuMet);b) In a similar arrangement, the relationship between the steep-to-gentle transition (*f*V) with the gold grade, metal content, and the aggregate gold resources (AuMet) is detailed;c) The sequence continues to demonstrate the association between the slope angle (*gF*) and gold grade, metal content, and the aggregate gold resources (AuMet);d) Lastly, from top to bottom, the correlation between trend undulation (*wa*F) with gold grade, metal content, and the total gold resources (AuMet) is presented.

4.4. Target Appraisal

The spatial attributes, specifically *dF*, *gF*, *waF*,*f*V, of labeled voxels (classified as either mineralized or non-mineralized) serve as inputs for the training of a Multilayer Perceptron (MLP). To assess the MLP's efficacy, divide the sample according to the ratio of 2:8 to obtain the validation set and training set.

This approach enables the MLP model to accurately predictive models within the Nibao Carlin-type gold deposit. The hyperparameters of the model are detailed in the accompanying table, providing a comprehensive overview of the settings optimized for this specific predictive task.

Table 2. Nibao Gold deposit Deep Prediction Training Parameters Table.

	Hidden Layer Structure	Optimization Algorithm	Maximum Iterations	Learning Rate	L2 Regularization Parameter /α
MLP	[90,90,90,90]	ADAM	200	0.001	0.0002

The performance of the three-dimensional metallogenic model for Au metal amount, grade, was evaluated using a set of metrics, including R^2 and validation set, Mean Squared Error (MSE), and Mean Absolute Error (MAE).

The results indicate that the R^2 values for the AuMet validation set are 0.768 and 0.796, respectively, suggesting that the ore control indicators can account for over 77% of the variability in the deep metal content of the Nibao Carlin-type gold deposit, and the model demonstrates a good overall fit. This implies a potentially strong relationship between Au metal content and ore control indicators within the deposit. The proximity of the training set R^2 to the test set R^2 signifies that the prediction model is not overfitted. The MSE and MAE between the predicted and actual values of Au metal content are 0.147 and 0.119, respectively, indicating the model's average deviation across each predicted three-dimensional unit. Although the model's predicted values generally align with the actual values, a slight discrepancy may exist for a minority of three-dimensional units with anomalously high values.

 doi:10.20944/preprints202404.1143.v1

For the Au grade, the test set R^2 and validation set values are 0.769 and 0.791, respectively, denoting a medium to high model fit and suggesting that the ore control index can explain between 76.9% and 79.1% of the variation in the grade mineralization index. This high level of model accuracy underscores the predictive model's reliability. The MSE and MAE between the predicted and actual Au grade values are 0.939 and 0.298, respectively, reflecting a minimal prediction error and attesting to the model's effective regression capability. In summary, the Multilayer Perceptron prediction model exhibits a commendable fitting effect, rendering its predictive outcomes valuable for reference.

The efficacy of the Multilayer Perceptron (MLP) model was validated using the Receiver Operating Characteristic (ROC) curve, focusing on the indicator analysis data from the Nibao Gold deposit validation set. The evaluation yielded compelling results: the ROC curve revealed an ROC value of 0.96 for the Nibao gold deposit's minerality prediction model, indicating that a smaller prediction area could achieve a higher degree of precision. Consequently, the MLP model demonstrates robust predictive capability for the three-dimensional deep resource forecasting within the Nibao Gold deposit.

Informed by the comprehensive database on grade, metal content, and mineralization predictions for the Nibao Carlin-type gold deposit in southwestern Guizhou, and grounded in geological expertise and patterns, prospective target areas were delineated. The prediction results served as the foundational criteria for confirming the boundaries of the target area, adhering to the principles of minimal volume, elevated grade, and significant metal content. Practical application predominantly utilized the Au grade prediction outcomes, earmarking prediction units with an Au predicted grade $\geqslant$ 1. Further refinement applied the ore posterior probability threshold (around 0.25), derived from the ore prediction curve's inflection point. Ultimately, according to established principles, the metal amount prediction results were leveraged as supplementary references to optimize the target volume and contour of the target area.

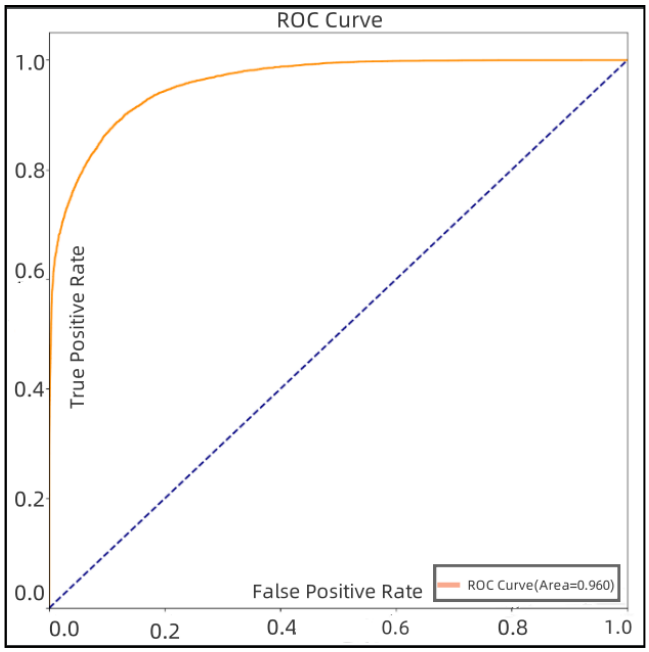

Figure 8. ROC curves for the training and validation sets of the MLP prospectivity model.

MLP prediction results showed that potential mineralization and known mineralizationcomprise an overall SW- to NE-striking gold zone at elevations from about –210to –790m.

 doi:10.20944/preprints202404.1143.v1

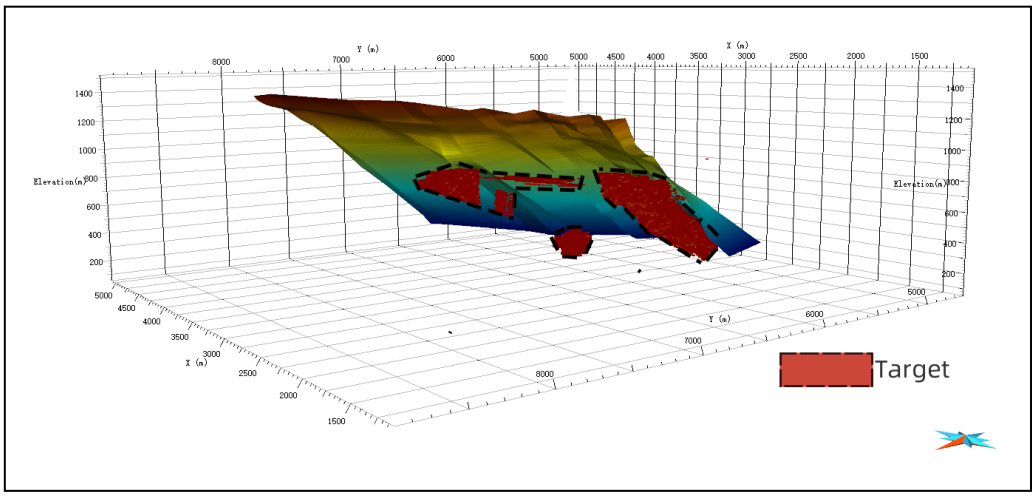

Figure 9. The prospectivity model of the Nibao deposit highlights the favorable areas for gold mineralization.

5. Discussion

Deposit structural scale of ore deposits is believed to directly control the distribution of gold mineralization and associated alteration and veining in the Nibao Carlin-type gold deposit. The results of three-dimensional modeling and spatial analysis revealed multiple peaks of high gold grade and cumulative gold content (AuMet) within the Nibao fault buffer zone, including a wide peak of consistent but lower gold grade between -380~80m, and high-grade peaks at 20~100m with 25-38 grams per ton. These observations suggest that the main gold ore bodies are located within 100 meters of the Nibao fault（Figure 3b）. The distribution of gold (Au) content within F1 shows variability, with higher concentrations in the southwestern part of the three-dimensional model area, especially at the intersection of F1, Sbt, and the anticlinal axis, where gold grades are relatively high, decreasing from WS to NE. Undulation analysis indicates that most ore bodies are associated with undulating parts of the Nibao fault, within a waF range of -10~20m(Figure 3c), indicating that mineralizing fluids concentrated within the bedding-parallel walls at the fault interface. According to the slope index gf(Figure 3d), the strain and differential stress along the vertical direction of the Nibao fault caused most of the ore-bearing fluids to stagnate in the flat sections below the fault. A small amount of fluid escaped to expansion areas through joints or folds related to compression, forming distal sub-vertical veins or branches of the main ore body. The combination of the Yangtze and Cathaysia blocks between 130ma-160ma, and the NanpanJiang foreland basin at the southwestern margin of the Yangtze Plate due to the subduction effects related to the Pacific Plate, brought magma up along crustal-scale faults. Ore-bearing hydrothermal fluids moved along slip structures between lithological interfaces with significant competency contrasts, such as $P_3l/P2_m$ and unconformities. This spatial angular change enhanced fluid stagnation, notably the degree of dip angle change (fV) indicates that many ore body units are located where the main fault plane's dip angle changes are minimal (-15-3°), affecting the extent of distal ore bodies less than proximal ore bodies at the same elevation (Figure 3a), suggesting that local changes in dip angle have a greater impact on high-grade ore bodies.

Previous studies suggest that the Nibao gold deposit's materials originate from the Emeishan mantle plume and deep magma sources [60–62]. The fluid primarily derives from deep magmatic water, incorporating formation water, metamorphic fluids, and atmospheric precipitation during its ascent [63–66]. As the ore-forming fluid ascends, its osmotic pressure gradually diminishes, and gold is precipitated under high confining pressure [67]. Integrating prior research with 3D models, it is hypothesized that deep Au-bearing hydrothermal fluids migrate upwards along deep faults, entering the sub-fault F1, and upon reaching the hanging wall contact point with $P2_m$, encounter lithologies of brecciated limestone and siliceous rock with poor permeability, while the footwall, in contact with

 doi:10.20944/preprints202404.1143.v1

Sbt, P_3l^1, and P_3l^2, consists of brecciated tuff and other materials with good permeability. Here, the overpressure fluid's osmotic pressure is released, facilitating mineralization and Au enrichment within Sbt, P_3l^1, and P_3l^2 in F1's footwall, while some fluid continues to ascend along the F1 fracture zone. The formation of F1 and Erlongqiangbao anticlines results in differing permeabilities between the upper and lower walls of F1, with the footwall exhibiting reduced porosity due to compaction. In contrast, the hanging wall, undergoing detachment and folding, develops favorable conditions for fluid erosion due to increased porosity and permeability, particularly along the anticline axis [23,61].

Analysis of the 3D model reveals ore bodies within the P_3l^1 and P_3l^2 formations, F1 fracture zone, and Erlongqiangbao anticline in F1's footwall, where the slope, trend undulations, and transitions between steep and gentle sections distinctly suggest that ore body formation is constrained by fluid migration, formation lithology, faults, and anticlines. Consequently, when overpressure Au-bearing fluids from deep sources migrate along major faults and enter reverse faults, ore bodies are likely to form within permeable strata of the reverse faults' footwall, Sbt, fracture zones of reverse faults, and anticlines, marking these spatial areas as advantageous sites for Au mineralization.

6. Conclusions

In this research, we developed a 3D model of the F1 fault and ore body within the Nibao gold deposit, thereafter delineating the fault's geometric characteristics and their association with gold mineralization. The quantitative findings indicate that gold mineralization within the Nibao gold deposit predominantly resides in proximity to the Nibao fault, spanning from -80 to 20 meters, with dip angles ranging from 20 to 45 degrees. The manifestation of varied gold mineralization styles is intricately influenced by the proximity and structural configuration of the Nibao fault. Data from exploration reports alongside the 3D model of the Nibao fault reveal that the Indosinian orogenic compression initially established the northeast-trending structural framework of the mining area, subsequently overlaid by northwest-trending structures during the Yanshanian orogenic compression. The regional stress transition from compressive to extensive forces initiated forward sliding movements in the F1 fault, creating tension spaces favorable for the ascent of deep ore-forming fluids and gold precipitation.

Upon applying regression analysis through a multilayer perceptron (MLP) model and mapping the prediction results back to the spatial context, targeted exploration depths are identified along lines 9340-9700 (with elevations ranging from 210m to 790m), 9980-10380 (elevations of 200m to 310m and 610m to 790m), and 9820-10060 (elevations of 455m to 780m). The ore body associated with the F1 fault exhibits a westward geometric orientation. The western section's deep edge and the southeast deep footwall of the F1 fault are earmarked as prospective directions for future mineral exploration.

These insights underscore the utility of multilayer perceptrons (MLP) in concert with exploration data and 3D prospecting modeling—encompassing 3D construction, spatial analysis, and deep learning—to profoundly enrich our understanding of the spatial dynamics between gold mineralization and geological structures. This approach proves instrumental in delineating fluid flow directions and pinpointing potential zones of mineralization deep within China's Carlin-type gold systems.

Author Contributions: Conceptualization, X.M. and H.G.; experiments, H.G.; writing—original draft preparation, H.G.; writing—review and editing, X.M., J.H., All authors have read and agreed to the published version of the manuscript.

Funding: This research is supported by projects from National Key R&D Program of China (No. 2023YFC2906404) and the Science and Technology Innovation Program of Hunan Province (2021RC4055).

Acknowledgments: Zhankun Liu is thanked for his suggestions for this paper.

Conflicts of Interest: The authors declare no conflict of interest.

References

1. Muntean J L, Cassinerio M D, Arehart G B, et al. Fluid pathways at the Turquoise Ridge Carlin-type gold deposit, Getchell district, Nevada[C]//Smart Science for Exploration and Mining, Proceedings of the Tenth

 doi:10.20944/preprints202404.1143.v1

Biennial Meeting of the Society of Geology Applied to Mineral Deposits, Townsville, Australia. 2009: 251-252.
2. Hofstra A H, Cline J S. Characteristics and models for Carlin-type gold deposits[J]. 2000.
3. Cline J S, Hofstra A A. Ore-fluid evolution at the Getchell Carlin-type gold deposit, Nevada, USA[J]. EUROPEAN JOURNAL OF MINERALOGY-STUTTGART-, 2000, 12(1): 195-212.
4. Goldfarb, R.J.; Santosh, M. The dilemma of the Jiaodong gold deposits: Are they unique? *Geosci. Front.* **2014**, *5*, 139–153.
5. Radtke A S, Rye R O, Dickson F W. Geology and stable isotope studies of the Carlin gold deposit, Nevada[J]. Economic Geology, 1980, 75(5): 641-672.
6. Kuehn C A, Rose A W. Carlin gold deposits, Nevada; origin in a deep zone of mixing between normally pressured and overpressured fluids[J]. Economic Geology, 1995, 90(1): 17-36.
7. Hofstra A H, Cline J S. Characteristics and models for Carlin-type gold deposits[J]. 2000..
8. Lamb J B, Cline J. Depths of formation of the Meikle and Betze/Post deposits[J]. 1997..
9. Cline J S, Hofstra A H, Muntean J L, et al. Carlin-type gold deposits in Nevada: Critical geologic characteristics and viable models[J]. 2005.
10. Hofstra A H, Snee L W, Rye R O, et al. Age constraints on Jerritt Canyon and other Carlin-type gold deposits in the Western United States; relationship to mid-Tertiary extension and magmatism[J]. Economic Geology, 1999, 94(6): 769-802.
11. Keith M, Smith D J, Jenkin G R T, et al. A review of Te and Se systematics in hydrothermal pyrite from precious metal deposits: Insights into ore-forming processes[J]. Ore Geology Reviews, 2018, 96: 269-282.
12. Groves D I, Goldfarb R J, Gebre-Mariam M, et al. Orogenic gold deposits: a proposed classification in the context of their crustal distribution and relationship to other gold deposit types[J]. Ore geology reviews, 1998, 13(1-5): 7-27.
13. Su W, Dong W, Zhang X, et al. Carlin-type gold deposits in the Dian-Qian-Gui "Golden Triangle" of southwest China[J]. 2018.
14. Xie Z, Xia Y, Cline J S, et al. Are there Carlin-type gold deposits in China? A comparison of the Guizhou, China, deposits with Nevada, USA, deposits[J]. 2018.
15. Mao, X., Ren, J., Liu, Z., Chen, J., Tang, L., Deng, H., et al. (2019). Three-dimensional prospectivity modeling of the Jiaojia-type gold deposit, Jiaodong Peninsula, Eastern China:A case study of the Dayingezhuang deposit. Journal of Geochemical Exploration, 203, 27–44.
16. Payne C E, Cunningham F, Peters K J, et al. From 2D to 3D: Prospectivity modelling in the Taupo volcanic zone, New Zealand[J]. Ore Geology Reviews, 2015, 71: 558-577.
17. Mao X, Ren J, Liu Z, et al. Three-dimensional prospectivity modeling of the Jiaojia-type gold deposit, Jiaodong Peninsula, Eastern China: A case study of the Dayingezhuang deposit[J]. Journal of Geochemical Exploration, 2019, 203: 27-44.
18. Mao X, Zhang B, Deng H, et al. Three-dimensional morphological analysis method for geologic bodies and its parallel implementation[J]. Computers & Geosciences, 2016, 96: 11-22.
19. Xia Y, Su W, Zhang X, et al. Geochemistry and metallogenic model of carlin-type gold deposits in southwest Guizhou province, China[J]. Geochemistry-Earth's System Processes; Panagiotaras, D., Ed, 2012: 127-156.
20. Su W, Dong W, Zhang X, et al. Carlin-type gold deposits in the Dian-Qian-Gui "Golden Triangle" of southwest China[J]. 2018.
21. Fu-xin Z, Li X, Ya-lin Q I. Exploration and study of Carlin and Carlin-like type gold deposits: review and prospect[J]. Geology in china, 2004, 31(4): 407-412.
22. Xie Z, Xia Y, Cline J S, et al. Are there Carlin-type gold deposits in China? A comparison of the Guizhou, China, deposits with Nevada, USA, deposits[J]. 2018.
23. Song W, Zheng L, Liu J, et al. Genesis, metallogenic model, and prospecting prediction of the Nibao gold deposit in the Guizhou Province, China[J]. Acta Geochimica, 2023, 42(1): 136-152.
24. Li J, Wu P, Xie Z, et al. Alteration and paragenesis of the basalt-hosted Au deposits, southwestern Guizhou Province, China: Implications for ore genesis and exploration[J]. Ore Geology Reviews, 2021, 131: 104034.
25. Xia Y, Su W, Zhang X, et al. Geochemistry and metallogenic model of carlin-type gold deposits in southwest Guizhou province, China[J]. Geochemistry-Earth's System Processes; Panagiotaras, D., Ed, 2012: 127-156.
26. Cline J S. Timing of gold and arsenic sulfide mineral deposition at the Getchell Carlin-type gold deposit, north-central Nevada[J]. Economic Geology, 2001, 96(1): 75-89.
27. Wu Z, Song S, Khosla A, et al. 3d shapenets: A deep representation for volumetric shapes[C]//Proceedings of the IEEE conference on computer vision and pattern recognition. 2015: 1912-1920.
28. Pour A B, Hashim M. Structural geology mapping using PALSAR data in the Bau gold mining district, Sarawak, Malaysia[J]. Advances in Space Research, 2014, 54(4): 644-654.
29. Malan, DF, Vogler, UW & Drescher K. Time-dependent behaviour of hard rock in deep level gold mines[J]. Journal of the Southern African Institute of Mining and Metallurgy, 1997, 97(3): 135-147.
30. Tripp G I, Vearncombe J R. Fault/fracture density and mineralization: a contouring method for targeting in gold exploration[J]. Journal of Structural Geology, 2004, 26(6-7): 1087-1108.

31. Carr J C, Beatson R K, Cherrie J B, et al. Reconstruction and representation of 3D objects with radial basis functions[C]//Proceedings of the 28th annual conference on Computer graphics and interactive techniques. 2001: 67-76.
32. Houlding S. 3D geoscience modeling: computer techniques for geological characterization[M]. Springer Science & Business Media, 2012.
33. Xiang, J., Xiao, K., Carranza, E. J. M., Chen, J., & Li, S. (2019). 3D mineral prospectivity mapping with random forests: A case study of Tongling, Anhui China. Natural Resources Research, 29(1), 395–414.
34. Xiao, K. Y., Li, N., Alok, P., Holden, E. J., Leon, B., & Lu, Y. J. (2015). GIS-based 3D prospectivity mapping: A case study of Jiama copper-polymetallic deposit in Tibet, China. Ore Geology Reviews, 71, 611–632.
35. Li N, Bagas L, Li X, et al. An improved buffer analysis technique for model-based 3D mineral potential mapping and its application[J]. Ore Geology Reviews, 2016, 76: 94-107.
36. Mao, X.; Ren, J.; Liu, Z.; Chen, J.; Tang, L.; Deng, H.; Bayless, R.C.; Yang, B.; Wang, M.; Liu, C. Three-dimensional prospectivity modeling of the Jiaojia-type gold deposit, Jiaodong Peninsula, Eastern China: A case study of the Dayingezhuang deposit. *J. Geochem. Explor.* **2019**, *203*, 27–44. https://doi.org/10.1016/j.gexplo.2019.04.002.
37. Allibone A, Teasdale J, Cameron G, et al. Timing and structural controls on gold mineralization at the Bogoso gold mine, Ghana, West Africa[J]. Economic Geology, 2002, 97(5): 949-969.
38. Qiu, Y.; Groves, D.I.; McNaughton, N.J.; Wang, L.-g.; Zhou, T. Nature, age, and tectonic setting of granitoid-hosted, orogenic gold deposits of the Jiaodong Peninsula, eastern North China craton, China. *Miner. Depos.* **2002**, *37*, 283–305. https://doi.org/10.1007/s00126-001-0238-3.
39. Liu, Z.-K.; Mao, X.-C.; Wang, F.-Y.; Tang, L.; Chen, G.-H.; Chen, J.; Deng, H. Deciphering anomalous Ag enrichment recorded by galena in Dayingezhuang Au(-Ag) deposit, Jiaodong Peninsula, Eastern China. *Trans. Nonferrous Met. Soc. China.* **2021**, *31*, 3831−3846.
40. Yang, L.Q.; Deng, J.; Guo, R.P.; Guo, L.N.; Wang, Z.L.; Chen, B.H.; Wang, X.D. World-class Xincheng gold deposit: An example from the giant Jiaodong gold province. *Geosci. Front.* **2016**, *7*, 419–430. https://doi.org/10.1016/j.gsf.2015.08.006.
41. Shen, K.; Hu, S.X.; Sun, J.G.; Ling, H.F.; Zhao, Y.Y.; Sun, M.Z. Characteristics of ore-forming fluids of the Dayingezhuang gold deposit in Eastern Shandong, China. *Acta Petrol. Sin.* **2000**, *16*, 542–550.
42. Mao, X.; Zhao, Y.; Deng, H.; Zhang, B.; Liu, Z.; Chen, J.; Zou, Y.; Lai, J. Quantitative analysis of intrusive body morphology and its relationship with skarn mineralization—A case study of Fenghuangshan copper deposit, Tongling, Anhui, China. Trans. Nonferrous Met. Soc. **2018**, 28, 151–162. https://doi.org/10.1016/S1003-6326(18)64648-5.
43. Zhang Q, Chen J, Xu H, et al. Three-dimensional mineral prospectivity mapping by XGBoost modeling: A case study of the Lannigou gold deposit, China[J]. Natural Resources Research, 2022, 31(3): 1135-1156.
44. Rodriguez-Galiano V, Sanchez-Castillo M, Chica-Olmo M, et al. Machine learning predictive models for mineral prospectivity: An evaluation of neural networks, random forest, regression trees and support vector machines[J]. Ore Geology Reviews, 2015, 71: 804-818.
45. Chi G, Xu D, Xue C, et al. Hydrodynamic links between shallow and deep mineralization systems and implications for deep mineral exploration[J]. Acta Geologica Sinica-English Edition, 2022, 96(1): 1-25.
46. Yousefi M, Kamkar-Rouhani A, Carranza E J M. Geochemical mineralization probability index (GMPI): a new approach to generate enhanced stream sediment geochemical evidential map for increasing probability of success in mineral potential mapping[J]. Journal of Geochemical Exploration, 2012, 115: 24-35.
47. Ruck D W, Rogers S K, Kabrisky M. Feature selection using a multilayer perceptron[J]. Journal of neural network computing, 1990, 2(2): 40-48.
48. Popescu M C, Balas V E, Perescu-Popescu L, et al. Multilayer perceptron and neural networks[J]. WSEAS Transactions on Circuits and Systems, 2009, 8(7): 579-588.
49. Baum E B. On the capabilities of multilayer perceptrons[J]. Journal of complexity, 1988, 4(3): 193-215.
50. Rasamoelina A D, Adjailia F, Sinčák P. A review of activation function for artificial neural network[C]//2020 IEEE 18th World Symposium on Applied Machine Intelligence and Informatics (SAMI). IEEE, 2020: 281-286.
51. Xiong, Y., & Zuo, R. (2020). Recognizing multivariate geo-chemical anomalies for mineral exploration by combining deep learning and one-class support vector machine. Computers & Geosciences, 140, 104484.
52. Xiang, J., Xiao, K., Carranza, E. J. M., Chen, J., & Li, S. (2019) 3D mineral prospectivity mapping with random forests: A case study of Tongling, Anhui China. Natural Resources Research, 29(1), 395–414.
53. Fawcett T. An introduction to ROC analysis[J]. Pattern recognition letters, 2006, 27(8): 861-874.
54. Fawcett T. ROC graphs with instance-varying costs[J]. Pattern Recognition Letters, 2006, 27(8): 882-891.
55. Muschelli III J. ROC and AUC with a binary predictor: a potentially misleading metric[J]. Journal of classification, 2020, 37(3): 696-708.
56. Vuk M, Curk T. ROC curve, lift chart and calibration plot[J]. Metodoloski zvezki, 2006, 3(1): 89.

 doi:10.20944/preprints202404.1143.v1

57. Mas J F. Receiver operating characteristic (ROC) analysis[J]. Geomatic approaches for modeling land change scenarios, 2018: 465-467.
58. Ye Z, Kesler S E, Essene E J, et al. Relation of Carlin-type gold mineralization to lithology, structure and alteration: Screamer zone, Betze-Post deposit, Nevada[J]. Mineralium Deposita, 2003, 38: 22-38.
59. Yang L, Deng J, Groves D I, et al. Recognition of two contrasting structural-and mineralogical-gold mineral systems in the Youjiang basin, China-Vietnam: Orogenic gold in the south and Carlin-type in the north[J]. Geoscience Frontiers, 2020, 11(5): 1477-1494.
60. Nie A. The study on the genetic mechanism of carlin-type gold deposit which caused by activity of Emei mantle plume in southwestern Guizhou[J]. 2009.
61. Song W, Zheng L, Liu J, et al. Genesis, metallogenic model, and prospecting prediction of the Nibao gold deposit in the Guizhou Province, China[J]. Acta Geochimica, 2023, 42(1): 136-152.
62. Li J, Wu P, Xie Z, et al. Alteration and paragenesis of the basalt-hosted Au deposits, southwestern Guizhou Province, China: Implications for ore genesis and exploration[J]. Ore Geology Reviews, 2021, 131: 104034.
63. Xianyang X, Dingsu F, Maohong C, et al. Fluid inclusion and stable isotope geochemistry study of the Nibao gold deposit, Guizhou and insights into ore genesis[J]. Acta Petrologica Sinica, 2016, 32(11): 3360-3376.
64. Zheng L, Yang R, Gao J, et al. Quartz Rb-Sr isochron ages of two type orebodies from the Nibao Carlin-type gold deposit, Guizhou, China[J]. Minerals, 2019, 9(7): 399.
65. Jin X, Yang C, Liu J, et al. Source and evolution of the ore-forming fluids of Carlin-type gold deposit in the Youjiang Basin, South China: Evidences from solute data of fluid inclusion extracts[J]. Journal of Earth Science, 2021, 32(1): 185-194.
66. Jin X Y, Zhao J X, Feng Y X, et al. Calcite U-Pb dating unravels the age and hydrothermal history of the giant Shuiyindong Carlin-type gold deposit in the golden triangle, South China[J]. Economic Geology, 2021, 116(6): 1253-1265.